Uncovering the Role of Electronic Doping In Lead-free Perovskite $(CH_3NH_3)_2CuCl_{4-x}Br_x$ and Solar Cells Fabrication

Mahdi Gassara[a], Naveen Harindu Hemasiri [b], Samrana Kazim[b,c], Ferdinando Costantino[d],Houcine Naïli[a] and Shahzada Ahmad*[b,c]

[a]Laboratoire Physico-chimie de l'Etat Solide, Département de Chimie, Faculté des Sciences de Sfax, B.P. 1171, 3000 Sfax, Université de Sfax, Tunisie.

[b]BCMaterials, Basque Center for Materials, Applications, and Nanostructures, Bld. Martina Casiano, UPV/EHU Science Park, Barrio Sarriena s/n, 48940 Leioa, Spain

Tel: +34 946128811, Email:shahzada.ahmad@bcmaterials.net

[c]IKERBASQUE, Basque Foundation for Science, Bilbao, 48009, Spain

[d]Department of Chemistry Biology and Biotechnologies University of Perugia Via Elce di Sotto 8, 06123 Perugia, Italy.

Abstract: Lead halide perovskites are attractive pigments to fabricate solar cells in the laboratory owing to their high power conversion efficiency. However, such materials also possess a high level of toxicity that is carcinogenic for humans and aquatic life due to the presence of Pb. Arguably, this hampers their acceptability for immediate commercialization. Here, we report the synthesis of two-dimensional copper-based perovskite as an environmentally benign alternative to lead-based perovskites. We evaluated their optoelectronic properties and photovoltaic parameters. The $(CH_3NH_3)_2CuCl_{4-x}Br_x$ with X = 0.3 and 0.66 are derivatives of the stable MA_2CuCl_4. The single crystals and powders diffractograms suggest compositions with varying Cl/Br ratios and different bromine localization in the inorganic framework. We noted a narrow absorption for copper mixed halide perovskite with a bandgap from 2.85 − 2.65 eV related to the halide ratio variation (crystal color variation). Our findings demonstrate the impact of halide to optimize the stability of methyl-ammonium copper perovskite and provide an effective pathway to design eco-friendly perovskites for electrooptical application.

Introduction

Over the last decade, the power conversion efficiency (PCE) in hybrid lead halide perovskites solar cells (PSCs) has witnessed a significant jump and delivered breakthrough results.[1,2] After the pioneering works[3–5], high PCE has been demonstrated with methylammonium lead iodide ($CH_3NH_3PbI_3$)[6–10] and their composition owing to its long electron−hole diffusion length, high absorption coefficient, and low defect density. Moreover, the rise in PCE was rapid from 3.8% in 2009[4] to >25%.[11] On the other side, the toxicity and carcinogenic nature of lead (Pb) is a significant obstacle to regulators that prevents its use in practical applications. Due to the high environmental sensitivity of lead-based perovskite, Pb must be immediately replaced with ecologically safe alternatives.[12–14] The scientific community considers that substituting environmentally favorable elements for Pb in perovskites is a crucial step to address the toxicity. [15–18]

The metallic elements that can offer the substitution of Pb, mainly belong to the IVA group[19–24], such as tin (Sn^{2+}) and germanium (Ge^{2+}), the VA group elements, bismuth (Bi^{3+}) and antimony (Sb^{3+}), and also the transition metal such as cobalt (Co^{2+}), iron (Fe^{2+}), zinc (Zn^{2+}), and copper (Cu^{2+}).[25,26] Tin becomes one of the most investigated elements that can replace the Pb, owing to the nearly similar ionic radius and electronic configuration (Pb 1.49 Å, Sn 1.35 Å). Such merits of Sn are attractive to replace Pb without a significant change in crystal structure and loss in photovoltaic performance. The initial attempt of using Sn^{2+} for solar cell fabrication, produce a competitive PCE of 6% with $MASnI_3$[23], and with further optimization, it increases to up to 13% recently.[27,28] However, those results are still incomparable with Pb-based PSCs due to the large deficit in open-circuit voltage (V_{oc}).[29] Additionally, the instability of Sn rapid oxidation from the Sn^{2+} to the Sn^{4+} state should be taken into consideration. Thus the use of Sn is seen as a critical barrier that affects the reproducibility of PSCs and restricts its wide practical use.

Furthermore, Bi and Sb have been also studied as lead-free perovskite, by probing $MA_3Bi_2I_9$ and $AgBi_2I_7$ as light absorbers. The $MA_3Bi_2I_9$ thin film was homogeneous and PSCs yielded a PCE of 1.12% and 1.62% using conventional 2,2,7,7-tetrakis (*N,N*'-di-p-methoxyphenylamino)−9,9-spirobifluorene), Spiro-OMeTAD, and poly(3-hexylthiophene-2,5-diyl-(P3HT) as hole transporting materials[30]. The issue associated with Bi-based perovskite is their wide band gaps ($E_g \geq 2.1$ eV) that make these materials unsuitable for light harvesting.[28]

The development of innovative sustainable technologies based on eco-friendly, cost-effective, and earth-abundant materials naturally drives attention toward the transition metals, such as Fe^{2+}, Cu^{2+}, Zn^{2+}, and Co^{2+} as potential substitutes for lead [31–33,34]. Copper is one such tunable element and less harmful to nature. Besides that, the human body has between 1.4 and 2.1 mg of copper per kilogram of body weight, and it is also crucial for all living biological systems as a component of enzymes.[35] Copper-based perovskite as a light absorber is being exploited as a benign medium.

In a prelimanary work, two cupric bromide hybrid perovskites [36] were reported, $(p\text{-}FC_6H_5C_2H_4NH_3)_2CuBr_4$ and $(CH_3(CH_2)_3NH_3)_2CuBr_4$, for PSCs fabrication and measured a

PCE of 0.51% and 0.63%, respectively. Followed by this a 2-D layered copper perovskite with mixed halide $(MA)_2CuCl_2Br_2$ has been reported as light-harvester and yielded a lower PCE of 0.017%,[26] signifying the potential of Cu-based perovskites. However, the absorption coefficient and stability of Cu-based perovskites is far from optimized. A stable $(C_6H_4NH_2)CuBr_2I$-based solar cell with a PCE of 0.46% was reported [37] and further, Li et al.[38] showed $(C_6H_5CH_2NH_3)_2CuBr_4$ as a highly stable 2D perovskite with a PCE of 0.2%. Mixed cations copper-based perovskite[39] with a compositon of $MA_{2-x}Cs_xCu(Cl/Br)_4$ was synthesized and yielded a PCE of 4.6×10^{-4} % for pure MA cation and 7.2×10^{-4} % for mixed cation (MA/Cs).

As mentioned, mixed halides in a 2D copper-based perovskite, i.e. $(CH_3NH_3)_2CuCl_xBr_{4-x}$, play an extremely important role in properties determination than of pure halide perovskites. However, compared to the single crystal structure, the polycrystalline nature of the thin film still has drawbacks, such as low chemical durability, heavy defect density, and lower carrier diffusion length. In addition, Recent studies suggest that through the perovskite crystals and thin film thickness optimization the optoelectronic applications can be fine-tuned.[40]

Herein, we report the synthesis of new hybrid 2D Cu-based perovskite in the form of bulk crystal powder and thin films to study their optoelectronic properties. Two compounds of $MA_2CuCl_{4-x}Br_x$ were elaborated using a low concentration of bromine (X = 0.3 and 0.66), giving rise to two different occupancy rates in the inorganic framework. The purity and the stability of the crystalline structure were confirmed on single crystals, powders, and thin films, by the diffraction pattern. This demonstrates a strong orientation along the (c) axis direction and preferred (00l) and (020) diffraction peaks for each perovskite. The estimated band gap energies are in the range of 2.85 − 2.65 eV. For their integration into PSCs, we made thin-film characterization and investigated the electro-optical properties to investigate the impact of mixed halides on photovoltaic performance, and compared it to pure halide MA_2CuCl_4 and MA_2CuBr_4 as references. Through this investigation of several features in 2D lead-free perovskites, their application potential can be tremendously expanded.

Results and Discussion

The crystal structure consists of a 2D “perovskite cage” and is restricted by the geometric considerations of the empirical Goldschmidt tolerance factor (t) and octahedral factor (μ):

$$t = \frac{r_A + r_X}{\sqrt{2}(r_A + r_X)}$$

$$\mu = \frac{r_B}{r_X}$$

where r_A, r_B, r_X are the effective radii of A^+, B^{2+}, and X^- ions respectively.[41] Generally, the higher stability range of the three-dimensional perovskite structure is in the domain of $0.8 < t < 0.9$ and $0.442 < \mu < 0.895$ where mostly 3D perovskite can be represented with the AMX_3 formula.[42]

The methyl ammonium has an ionic radius r_{MA} = 180 pm and the $MACuCl_3$ perovskite has a tolerance factor, t = 1.004, and octahedral factor, μ = 0.403, such values are beyond the stability range and allow the formation of reduced dimensionality 2D-MA_2CuCl_4 perovskite structure.[26]

The crystal structures of $(CH_3NH_3)_2CuCl_{3.7}Br_{0.3}$ and $(CH_3NH_3)_2CuCl_{3.63}Br_{0.37}$ is similar to $(CH_3NH_3)_2MCl_4$ compounds (M = Mn, Cd, or Fe).[43] Although in the first scenario, it is necessary to consider the contribution made by the Jahn-Teller distortion (a property of the $3d^9$ Cu^{2+} ion): Contrasting with the other four shorts Cu—X distances, two of the four Cu—X bonds in equatorial position (displayed inside the inorganic plane) are significantly longer than the other four, which corresponds to the literature reports[44,45].

The X-ray diffraction (XRD) patterns of perovskite single crystals following solution synthesis (Figure S1) suggests the existence of two distinct crystal structures (Table S1). Meanwhile, $MA_2CuCl_{4-x}Br_x$ crystallize in monoclinic and orthorhombic systems for X = 0.3 and 0.6 respectively, were realized with the space groups $P2_1/a$ and A*bm2* (Table1). Figure 1b and Figure 2b present the $Cu(Cl/Br)_6$ octahedron, indicating the Cu—X (with X= Cl/Br) bond lengths. The slight difference in the bond length is mainly due to the various amount of bromine and the two different crystalline systems.

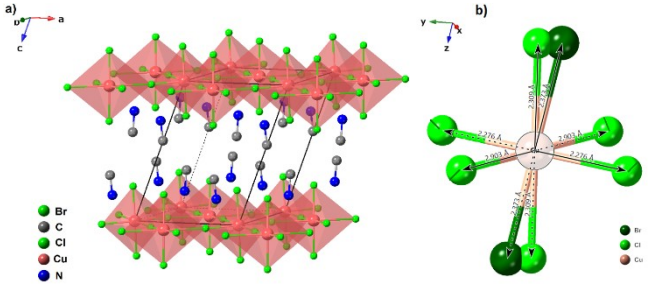

Figure 1. a) Representation of $MA_2CuCl_{3.7}Br_{0.3}$ crystal structure, b) the Cu−X bond lengths and halides Cl/Br position sharing in the inorganic framework.

The crystal structures of the various copper perovskites are based on a two-dimensional framework built by the $[CuX_6]^{4-}$ corner-sharing octahedra. This later generates stacked layers along the *c*-axis for X= 0.3 and along the *b*-axis for X= 0.66. Thus, resulting in a layer sequence of *ABAB*-type a with separating distances between the layers around 9.372 Å and 9.421 Å for X = 0.3 and 0.66, respectively. The low doping of bromine in the MA_2CuCl_4 causes the presence of different crystalline systems which is related to the increased bromine ratio (x = 0.3 to x = 0.66), resulting in a structural change from the monoclinic to the orthorhombic crystalline system. [26,33] In the first compound, the bromine presents 7.5 % of the halide amount in the structure. In addition, it occupies all the positions in the $[CuCl_{3.7}Br_{0.3}]$ octahedral with two different ratios. The first position presents a proportion of 0.884 (4)/0.116 (2) for chloride and bromine respectively, with a distance Cu—Cl (2.308(29))<Cu-Br (2.375(94)). In the second position, the Cl_3/Br_3 proportion gives a value of 0.967(5)/0.033(5). Such results are observed in the asymmetric unit of each crystalline structure (Figure S2a, supporting information). However, in the second perovskite 16.5% of bromine of all halide amount is present in the structure. It shows a different distribution localized in three different positions of the octahedron with a ratio of Cl_2/Br_2 0.917(11)/0.083(11), Cl_3/Br_3 0.743(8)/0.257(8) and Cl_4/Br_4 0.934(17)/0.066(17), (Figure S2b, supporting information).

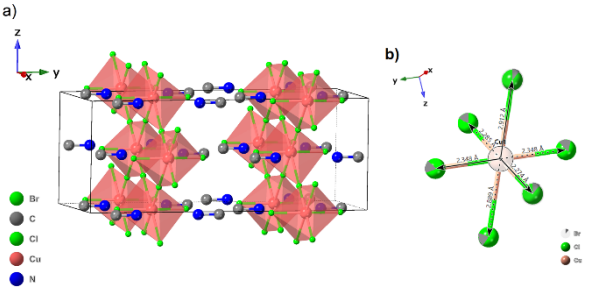

Figure 2. Representation of $MA_2CuCl_{3.34}Br_{0.66}$ crystal structure, b) the Cu−X bond lengths and halides Cl/Br position sharing in the inorganic framework.

Table 1. Structure parameters of $(CH_3NH_3)_2CuCl_{4-x}Br_x$ (X = 0.3 and 0.66).

Perovskites	Space group	a (Å)	b (Å)	c (Å)	β (deg°)
$MA_2CuCl_{3.7}Br_{0.3}$	$P2_1/a$	7.289	7.356	10.039	111.19
$MA_2CuCl_{3.34}Br_{0.66}$	Abm2	7.302	7.347	10.089	111.15

The developed layered perovskites can be deposited as thin films using a dimethyl formamide (DMF) as a solvent. Firstly, we selected MA_2CuCl_4, $MA_2CuCl_{3.7}Br_{0.3}$, and $MA_2CuCl_{3.34}Br_{0.66}$ for stability optimization and to tune their optical properties. The diffraction patterns of MA_2CuCl_4 thin film (Figure 3), and $CuCl_2$ and MACl as references show a strong preferential orientation toward the 001 direction, with the organic and inorganic layers parallel to the substrate, presenting the crystalline phases of $(CH_3NH_3)_2CuCl_4$.[43]

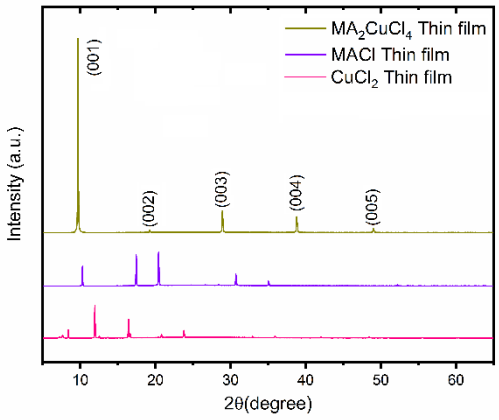

Figure 3. X-ray diffraction patterns of $(MA)_2CuCl_4$, $CuCl_2$, and MACl thin film.

Additionally, XRD patterns were used also to decipher the synthetic MA_2CuCl_4 powder structure in comparison to $CuCl_2$, and CH_3NH_3Cl (methyl-ammonium chloride) (Figure 3), suggesting no raw material residues were found under the X-rays detection limit. The diffraction peaks at 2θ of 9.67°, 19.25°, 29.65°, 38.81°and 49° are assigned, respectively, to the planes: (001), (002), (003), (004), and (005). Monoclinic copper chloride is noted as similar to the earlier report of MA_2CuCl_4.[26]. Furthermore, we used a similar method to unravel the synthesis of MA_2CuBr_4 and compared it with copper bromide ($CuBr_2$) and methylammonium bromide (MABr). The MA_2CuBr_4 diffraction pattern (Figure S3) reveals a compatible structure with the orthorhombic crystal system. [33,46]

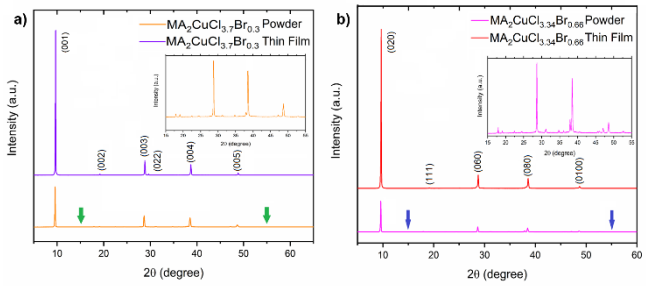

Figure 4. Comparison of X-ray diffraction of $MA_2CuCl_{3.7}Br_{0.3}$ and $MA_2CuCl_{3.34}Br_{0.66}$ for powder crystal and thin film respectively.

Furthermore, the powder X-ray of $MA_2CuCl_{3.7}Br_{0.3}$ and $MA_2CuCl_{3.34}Br_{0.66}$ when compared to the thin film X-ray pattern (Figure 4), suggests no remnants of raw materials. The diffraction peaks (Figure 4) reveal different planes in both the perovskites with strong orientation for 001 and 020 for $MA_2CuCl_{3.7}Br_{0.3}$ and $MA_2CuCl_{3.34}Br_{0.66}$, respectively. The results related to the existing two different crystalline systems can also be identified by the single crystals X-ray diffraction (Figure S4). The thin film diffraction pattern presents a similar orientation to the 001 direction for $MA_2CuCl_{3.7}Br_{0.3}$ and the 020 direction for $MA_2CuCl_{3.34}Br_{0.66}$. The systematic change from a single crystal, powder, and thin films is used to verify the crystalline structure and perovskite stability. [26,33,39,43].

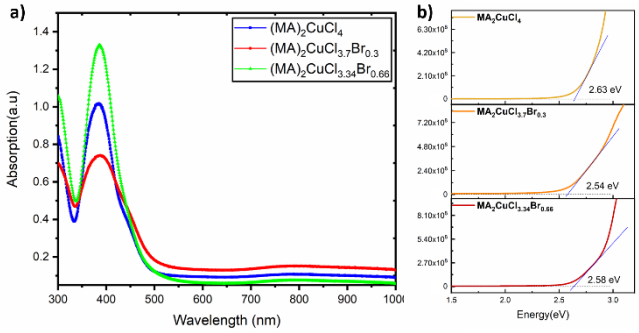

Figure 5. UV-vis spectrum and Tauc plots for the determination of band gaps associated with charge transfer (CT) of MA_2CuCl_4, $MA_2CuCl_{3.7}Br_{0.3}$, and $MA_2CuCl_{3.34}Br_{0.66}$.

The absorption spectra of the series MA_2CuCl_4, $MA_2CuCl_{3.7}Br_{0.3}$, and $MA_2CuCl_{3.34}Br_{0.66}$ show typical features of the CuX_4^{2-} in square planar coordination for copper complexes.[49] The maximum absorption peak at 341 nm and 343.25 nm is attributed to $MA_2CuCl_{3.7}Br_{0.3}$ and $MA_2CuCl_{3.34}Br_{0.66}$, respectively (Figure 5a). The corresponding band gap from Tauc plots (Figure 5b) is determined to be 2.54 eV (477 nm) for MA_2CuCl_4, 2.65 eV (475 nm) for $MA_2CuCl_{3.7}Br_{0.3}$ and 2.58 eV (474 nm) for $MA_2CuCl_{3.34}Br_{0.66}$. Intriguingly, the second peak of absorption appears in the visible below the band gap, with weaker and wider bands between 650 and 900 nm (Figure S5a). These bands are mainly attributed to the d level of copper (Cu^{2+}) and it shows a constant absorption for the perovskites tree, and with the various Cl/Br ratio in the structure. The Gauss fitting scenario of optical absorption (Figure S5b, supporting information) demonstrates the presence of two ligands to metal charge transfer (LMCT) transition exhibited by this perovskite. This transition is suggested

in the previous copper chloride perovskite. [26,31,32] The two transitions at 379 nm and 441 nm can be attributed to Cl/Br (pσ) →Cu ($d_{x^2-y^2}$) and Cl/Br (pπ) → Cu ($d_{x^2-y^2}$). Moreover, the same fitting indicates the existence of three transitions between the d orbitals of Cu^{2+} such as Cu ($d_{xz, yz}$) → Cu ($d_{x^2-y^2}$), Cu (d_{xy}) → Cu ($d_{x^2-y^2}$), and Cu (d_{z^2}) → Cu ($d_{x^2-y^2}$). The different ratios of bromide in $MA_2CuCl_{4-x}Br_x$ affect slightly the optical properties of the thin films perovskite. With the increases in the Br content, the absorbance edge slightly shifts to short-wavelength values, resulting in a small variation of the band gap energy from 2.85 eV to 2.65 eV. The slight change in the optical band gap and the absorption for $MA_2CuCl_{3.7}Br_{0.3}$ is ascribed to the presence of the Br with a mixed occupancy in all halide positions of octahedral geometry coordination.[47,48] Additionally, we synthesized MA_2CuBr_4 which shows the maximum absorption up to 600 nm, and a corresponding band gap calculated from the Tauc plot is 1.42 eV (Figure S6). We noted MA_2CuBr_4 represents a short life when exposed to air, as the thin films were highly hygroscopic (Figure S7).

The bromine doping in MA_2CuCl_4 conserves the stability of the thin films for up to 10 days under atmospheric conditions. However, MA_2CuBr_4 has lower UV-vis absorption with the domination of LMCT transitions, and a high band gap compared to the other unstable methyl ammonium copper perovskite.[30,26,37]

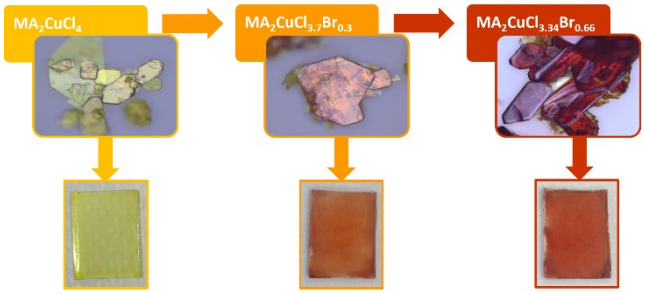

Figure 6. Optical microscope and photograph images showing the color shift of the material crystal and thin films with the different ratios of the Cl and Br halogen content: MA_2CuCl_4 (yellow), $MA_2CuCl_{3.7}Br_{0.3}$ (orange), and $MA_2CuCl_{3.34}Br_{0.66}$ (dark orange).

This modulation of the band gap can be visualized from the color of the crystal powders, which changes from yellow to dark brown color with the increase of the Br ratio (Figure 6).

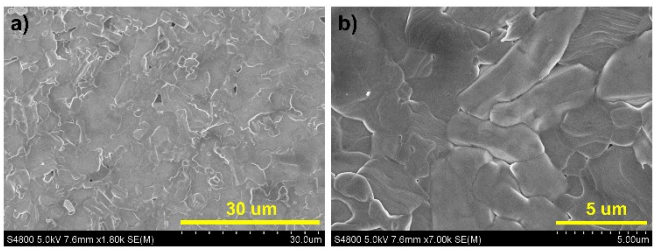

Figure 7. SEM image of $(MA)_2CuCl_{3.7}Br_{0.3}$ displaying the layered structure on, a) 30 µm scale, and b) 5 µm scale.

The surface microstructure of the perovskite thin film of 2D-$MA_2CuCl_{3.7}Br_{0.3}$ on the FTO substrate was performed with scanning electron microscopy (SEM). The microstructure (Figure 7a), suggests variation in grain size. The optimized concentration of 2 molars (2M) avoids the presence of a pinhole. The surface displays the layered structure of perovskite with different grain sizes and homogeneous distribution (Figure 7b).

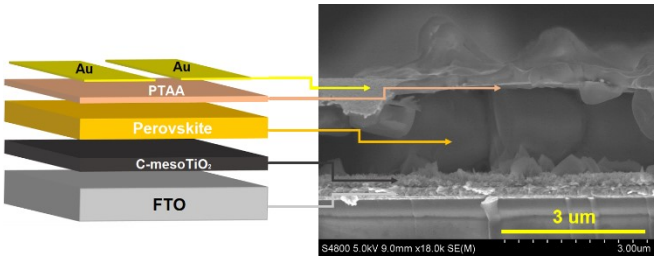

Figure 8. Scheme of PSCs adopted (n–i–p structure) and cross-sectional SEM image of the fabricated PSC.

We evaluated the photovoltaic performance with varied Br addition in $MA_2CuCl_{4-x}Br_x$ in a regular device architecture (Figure 8) of fluorine-doped tin oxide (FTO)/b&mp-TiO_2/$MA_2CuCl_{4-x}Br_x$/PTAA/Au. The cross-sectional scanning electron microscopy (SEM) of the PSC based on $MA_2CuCl_{3.7}Br_{0.3}$ shows a compact sandwich structure consisting of well-arranged perovskite large grains along the vertical direction (Figure 8), which is beneficial for photo-charge kinetics in the device. Poly(triaryl amine) PTAA in pristine form was used as the hole transport layer (HTL) for PSCs fabrication since additives and dopants can dissolve the perovskite layer. The device performance is tabulated in Table 2. The perovskites, transfer the electron upon the photoexcitation from the (mp-TiO_2) to the HTL. Due to the limited absorption of perovskite investigated here, higher thickness is crucial and we optimized the concentration in DMF solution and avoided any agglomeration on the surface. However, higher concentration increases the crystallization rate during the spin-coating process of the thin films and this can be an issue to deposit homogenous and uniform layers. In this work, we obtained good-quality thin films due to solvent optimization.[27,37–39]

Table 2. Photovoltaic parameters of $MA_2Cl_{4-x}Br_x$ perovskite (X = 0.3 and 0.66).

Solar Cells	Scan	V_{OC} (mV)	J_{SC} (mA cm^{-2})	FF (%)	PCE (%)
MA_2CuCl_4	RS	107.76	0.3245	32.99	0.0115
	FS	87.86	0.0821	25.84	0.0019
$MA_2CuCl_{3.7}Br_{0.3}$	RS	170.96	0.1472	28.06	0.0071
	FS	167.43	0.1148	28.74	0.0055
$MA_2CuCl_{3.34}Br_{0.66}$	RS	116.34	0.1877	29.22	0.0064
	FS	108.02	0.1112	23.93	0.0029

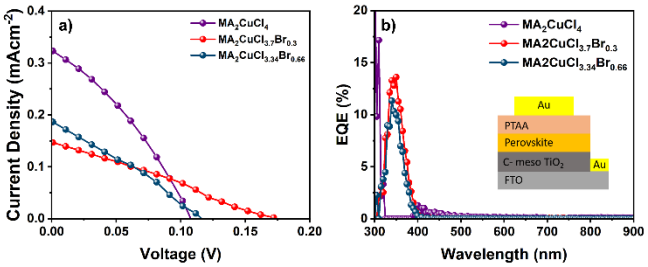

Figure 9. a). *J–V* curve of the PSCs fabricated using MA_2CuCl_4, $MA_2CuCl_{3.7}Br_{0.3}$, $MA_2CuCl_{3.34}Br_{0.66}$, and b) the corresponding EQE spectrum.

The PSCs fabricated (Figure 9a) with MA_2CuCl_4 exhibited a PCE of 0.0115 % (J_{sc} = 0.32 mAcm^{-2}, V_{oc} = 107.76 mV FF= 33 %), while for the $MA_2CuCl_{3.7}Br_{0.3}$ based PSC yielded a PCE of 0.0071 % (J_{sc} = 0.147 mA.cm^{-2} V_{oc} = 170.96 mV, FF = 28%) and the $MA_2CuCl_{3.34}Br_{0.66}$ yielded a lower PCE of 0.0064 % (J_{sc} = 0.1877 mAcm^{-2}, V_{oc} = 116.34 mV, FF = 29.21 %). The bromine doping on the MA_2CuCl_4 structure conserves stability, while one of the goals of doping here is to optimize the light absorption and achieve a lower band gap to obtain a higher PCE. As a result, this substitution does not influence the energy gap and it gives a lower PCE comparable to the reference perovskite. The MA_2CuBr_4 exhibited a better PCE of 0.0229 % (J_{sc} = 0.160 mAcm^{-2}, V_{oc} = 585.14 mV, FF = 24.42%). However, it showed relatively rapid degradation of the absorber layers (Figure S9). The results suggest that the lower performance is due to the presence of bromine in the structure, which increases the presence of Cu^+ together with $CuCl_2$ in the perovskite thin films. The presence of the bromine raised the reduction process of PCE, on the contrary, the presence of chlorine improves the stability of the Cu^{2+} oxidation state. This is also supported by photoluminescence and X-ray photoelectron spectroscopy (XPS) studies.[26,50,51]

A similar composition was studied using ultraviolet photoelectron spectrum (UPS) to identify the Fermi energy (E_F) and the valence band maximum level. (VBM). The estimated VBM value of $MA_2CuCl_2Br_2$ (− 4.98 eV)[26]. While the HOMO of the PTAA was found to be -5.14eV.[52]

The measured external quantum efficiency (EQE) spectra of MA_2CuCl_4, $MA_2CuCl_{3.7}Br_{0.3}$, and $MA_2CuCl_{3.34}Br_{0.66}$ (Figure 9b) depict a narrow response in the region of visible 300−450 nm. The EQE spectra were obtained by using similar charge-selective layers, following the UV–vis absorption spectra due to the domination of the LMCT. All three PSCs do not show any EQE response at higher wavelengths longer than 400 nm (the absence of contribution of d-d transitions). We attribute this to the materials' inherent light absorption.

The calculated integrated J_{sc} from EQE data (Figure S10) is 0.0519, 0.0641, and 0.0456 mAcm^{-2} for, MA_2CuCl_4, $MA_2CuCl_{3.7}Br_{0.3}$, and $MA_2CuCl_{3.34}Br_{0.66}$ respectively, which are slightly lower than the J_{sc} values recorded from the *J–V* curves. This divergence is explained by the presence of shallow trap states at the perovskite/charge selective layer contacts[53] and is comparable to other Cu-based perovskite solar cells (Table S2)

The device's resistance typically influences the charge transport and the recombination of PSCs. To understand the charge-transfer kinetics of PSCs based on different $MA_2CuCl_{4-x}Br_x$, we performed the electrochemical impedance spectroscopy (EIS) under dark conditions at an applied voltage range of the working device between 0.08 − 0.12V (Figure 11). The recombination resistance (R_{rec}) for each device was extracted from the low-frequency region of the corresponding Nyquist plot fitted with an equivalent circuit model of R_s+R_{rec}||CPE (single-arc), where R_s is an overall series resistance including external resistance of connecting wires and electrodes, and CPE represent a constant phase element. The calculated recombination resistances are 20.40, 39.05, and 28.53 kΩ for MA_2CuCl_4, $MA_2CuCl_{3.7}Br_{0.3}$, and $MA_2CuCl_{3.34}Br_{0.66}$, respectively (Figure 10a). Higher recombination resistance is beneficial to suppress non-radiative recombination at the interfaces, which facilitates effective photo-charge kinetics in the PSCs.[54] The PSCs with $MA_2CuCl_{3.7}Br_{0.3}$ and $MA_2CuCl_{3.34}Br_{0.66}$ feature a higher R_{rec} than that of the control PSCs at a given potential bias (Figure 10b), indicating an enhanced resistance to charge annihilating and recombination at the interfaces. The fact that the recombination resistance in MA_2CuCl_4 and $MA_2CuCl_{3.34}Br_{0.66}$ are voltage-independent suggests that the recombination mechanism in both devices are comparable.

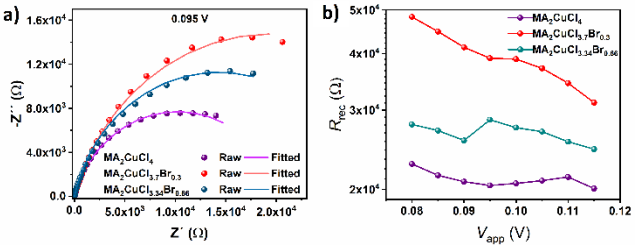

Figure 10. a) Electrochemical impedance spectra of PSCs measured for the tree perovskites at an applied voltage of 0.095 mV in the dark (raw and fitted data) and b) charge transport resistance,

The fabricated PSCs were probed for stabilized power output tracking using 1-sun illumination on the atmospheric conditions (55–70% RH at 27°C). After continuous MPP tracking for 500 seconds (Figure S12) the MA_2CuCl_4 and $MA_2CuCl_{3.7}Br_{0.3}$ PSCs show lower stability due to the significant decrease of the current, in 260 s for the first PSC and just 90 s for the second one respectively. For the layered perovskite structure, the poor out-of-plane charge transport is not beneficial for the transport and extraction of charge carriers in solar cells [55,56] and is a plausible reason for the low J_{sc}. Moreover, film quality is important to induce effective charge transport due to the inter-layer connection. Increasing the concentrations affects the grain size and that also caused the appearance of holes in the films (Figure S13), this deteriorates PSCs performance by forming shunt pathways.[57]

Conclusion

To summarize, we synthesize a new series of $MA_2CuCl_{4-x}Br_x$ perovskite with (x = 0.3 and 0.66) and investigated their structural, optical, and photovoltaic properties. The doping strategy gives a highly stable perovskite due to the low Br ratio. The optical properties suggest the impact of bromine on the band gap value and the domination of the ligand to metal charge transfer transition on the d-d transition. The development of copper perovskite-based solar cells gave an initial power conversion efficiency of 0.0115% for MA_2CuCl_4, 0.0071% for $MA_2CuCl_{3.7}Br_{0.3}$and 0.0064% $MA_2CuCl_{3.34}Br_{0.66}$. The optical absorptions are correlated with the external quantum efficiency

results, demonstrating the effect of the low absorption region on the PCE of those materials. Our findings provide new pathways for future research direction into stable and environmentally friendly hybrid perovskite materials.

Experimental Section

1. Synthesis of $MA_2CuCl_{4-x}Br_x$

Perovskite Nanocrystals powder of MA_2CuBr_4, MA2CuCl4, $MA_2CuCl_{3.7}Br_{0.3}$, and $MA_2CuCl_{3.34}Br_{0.66}$ were synthesized from methanol solutions. The precursors methyl-ammonium chloride (MACl, 99.99%, GreatCell Solar), methyl-ammonium bromide (MABr, 99.99%, GreatCell Solar), $CuCl_2$ (copper chloride, 99% Sigma-Aldrich) and $CuBr_2$ (copper bromide, 99% Sigma-Aldrich). The chemicals were mixed in the desired stoichiometry. For example, to synthesize $MA_2CuCl_{3.7}Br_{0.3}$, 0.134 g of $CuCl_2$, 0.118 g of MACl, and 0.027 g of MABr were mixed in 100 mL of MeOH, stirred for 2 h at 70 °C, and left to crystallize for 48 hours in an ice bath (0 °C). The powder crystals product was recovered by a rotary evaporator followed by washing the product with diethyl ether and drying at 65 °C for 12 h in a vacuum. Finally, the products are stored in an argon-filled glove box. The appearance of perovskite crystal is presented in Figure S1, supporting information.

2- Material Characterization.

Single crystal X-ray crystallographic

Single-crystal X-ray diffraction (XRD) data were collected using an APEX II, Bruker-AXS diffractometer with the Mo Kα radiation (λ=1.54184Å) at room temperature, 293K). The structure was solved with the direct method and refined by the full-matrix least-squares method based on F2 using the SHELXT software.

Thin-Film Characterization:

X-ray diffractograms were performed using a D8 Advance diffractometer from Bruker (Bragg–Brentano geometry, with an X-ray tube Cu, Kα, λ=1.5406 Å). The absorption spectra were measured using a UV-Vis spectrophotometer (Varian Cary 60 UV/Vis Spectrophotometer). The Morphological and compositional characterization was made with a field emission scanning electron microscope (FE-SEM) Jeol JSM-6700F.

3- Solar Cell Fabrication.

Fluorine-doped tin oxide (FTO) coated glasses (TEC7) were subsequently washed with a 2% solution of Hellmanex II, Milli-Q water, Acetone, and isopropanol in an ultrasonic bath for 20 min, followed by UV-ozone treatment for 45 min. Compact and mesoporous TiO_2 layers were deposited on freshly UV-ozone-treated substrates as reported in the previous report [58]. Briefly, a compact layer of TiO_2 was deposed by spray pyrolysis using a diluted 5% titanium(IV) diisopropoxide bis(acetylacetonate) solution at 500 °C and sintered for another 30 min at the same temperature. Mesoporous TiO_2 film was deposited by spin-coating a TiO_2 nanoparticle (30 NRD from Dyesol) dispersion (1:8 vw/v in anhydrous ethanol) at 4000 rpm for 30 s and annealed at 500 °C for 30 min. Perovskite deposition was conducted in an argon-filled glovebox under controlled oxygen and moisture conditions (H_2O level: <1 ppm and O_2 level: <5 ppm). Two molars (2M) concentration of perovskite solution was spin-coated at 3000 rpm for 30 s in a one-step deposition method followed by solvent engineering. During the last 10 s of the spinning process, 110 µL of chlorobenzene was dripped as an anti-solvent. The perovskite-coated substrates were annealed at 80 °C for 30 min. Once the substrates cooled down to room temperature, the PTAA (10 mg/mL in toluene solution) was deposited by spin-coating at 3000 rpm for the 30s.

To finish the device fabrication, a gold layer of 70 nm as a top contact was thermally evaporated under a low vacuum level (~10^{-6} torr).

Device Characterization:

Current density–voltage (*J–V*) curves were performed using an Oriel AAA solar simulator (Newport) producing 1 sun AM1.5G (100mW/cm^2) simulating sunlight and were recorded by applying an external potential bias to the devices. The generated photocurrent was recorded at a scan rate of 100 mV/s (pre-sweep delay: 10 s) with the help of a Keithley 2400 source meter and 0.09 cm^2 black metal mask as the active area. External quantum efficiency (EQE) measurements were carried out using a 150W xenon lamp attached to a Bentham PVE300-motorized 1/4m monochromatic as the light source. Electrochemical impedance measurements were performed in the frequency range of 2 MHz -1 Hz under the 20 mV perturbation using a Biologic SP-300 impedance analyzer inside a Faradaic chamber.

Acknowledgements

S.A. and S.K. acknowledge the funding received from the European Union H2020 program under the European Research Council Consolidator grant MOLEMAT (726360), and INTERACTION (PID2021-129085OB-I00) and ARISE (PID2019-111774RB-100), from the Spanish Ministry of Science and Innovation.

Keywords: perovskite • lead-free • cooper based perovskites • solar cells • eco-friendly

[1] P. V. Kamat, *J. Am. Chem. Soc.*, **2014**, 136, 3713–3714.
[2] R. Wang, T. Huang, J. Xue, J. Tong, K. Zhu and Y. Yang, *Nature Phot.* **2021**, 15, 411–425.
[3] H. S. Kim, C. R. Lee, J. H. Im, K. B. Lee, T. Moehl, A. Marchioro, S. J. Moon, R. Humphry-Baker, J. H. Yum, J. E. Moser, M. Grätzel and N. G. Park, *Scientific Reports*. **2012**, 2, 1–7.
[4] A. Kojima, K. Teshima, Y. Shirai and T. Miyasaka, *J. Am. Chem. Soc.* **2009**, 131, 6050–6051.
[5] Y. Zhou and M. Saliba, *ACS Energy Lett*, **2021**, 6, 2750–2754.
[6] W. Nie, H. Tsai, R. Asadpour, J. C. Blancon, A. J. Neukirch, G. Gupta, J. J. Crochet, M. Chhowalla, S. Tretiak, M. A. Alam, H. L. Wang and A. D. Mohite, *Science*. **2015**, 347, 522–525.
[7] M. Liu, M. B. Johnston and H. J. Snaith, *Nature*. **2013**, 501, 395–398.
[8] H. S. Kim, C. R. Lee, J. H. Im, K. B. Lee, T. Moehl, A. Marchioro, S. J. Moon, R. Humphry-Baker, J. H. Yum, J. E. Moser, M. Grätzel and N. G. Park, *Scientific Reports.* **2012**, 2, 1-7
[9] N. G. Park, *Materials Today*. **2015**, 18, 65–72.
[10] J. H. Im, C. R. Lee, J. W. Lee, S. W. Park and N. G. Park, *Nanoscale*. **2011**, 3, 4088–4093.
[11] M. Green, E. Dunlop, J. Hohl-Ebinger, M. Yoshita, N. Kopidakis and X. Hao, *Progress in Photovoltaics: Research and Applications*. **2021**, 29, 3–15.
[12] L. N. Quan, B. P. Rand, R. H. Friend, S. G. Mhaisalkar, T. W. Lee and E. H. Sargent, *Chem. Rev.* **2019**, 119, 7444–7477.
[13] A. Babayigit, A. Ethirajan, M. Muller and B. Conings, *Nat. Mater.* **2016**, 15, 247–251.
[14] M. G. Ju, J. Dai, L. Ma and X. C. Zeng, *J. Am. Chem. Soc.*. **2017**, 139, 8038–8043.
[15] Z. Shi, J. Guo, Y. Chen, Q. Li, Y. Pan, H. Zhang, Y. Xia and W. Huang, *Adv. Mater.* **2017**, 29, 1605005.
[16] T. Zhu, Y. Yang and X. Gong, *ACS Appl. Mater. Interfaces* **2020**, 12, 26776–26811.
[17] M. G. Ju, M. Chen, Y. Zhou, J. Dai, L. Ma, N. P. Padture and X. C. Zeng, *Joule*. **2018**, 2, 1231–1241.
[18] L. Liang and P. Gao, *Adv. Sci*., **2018**, 5, 1700331.

[19] P. Cheng, T. Wu, J. Zhang, Y. Li, J. Liu, L. Jiang, X. Mao, R. F. Lu, W. Q. Deng and K. Han, *J. Phys. Chem. Letters*. **2017**, 8, 4402–4406.

[20] I. Kopacic, B. Friesenbichler, S. F. Hoefler, B. Kunert, H. Plank, T. Rath and G. Trimmel, *ACS Applied Energy Mater*. **2018**, 1, 343–347.

[21] W. Ke, C. C. Stoumpos, I. Spanopoulos, L. Mao, M. Chen, M. R. Wasielewski and M. G. Kanatzidis, *J. Am. Chem. Soc.*. **2017**, 139, 14800–14806.

[22] Y. Liao, H. Liu, W. Zhou, D. Yang, Y. Shang, Z. Shi, B. Li, X. Jiang, L. Zhang, L. N. Quan, R. Quintero-Bermudez, B. R. Sutherland, Q. Mi, E. H. Sargent and Z. Ning, *J. Am. Chem. Soc.*. **2017**, 139, 6693–6699.

[23] N. K. Noel, S. D. Stranks, A. Abate, C. Wehrenfennig, S. Guarnera, A. A. Haghighirad, A. Sadhanala, G. E. Eperon, S. K. Pathak, M. B. Johnston, A. Petrozza, L. M. Herz and H. J. Snaith, *Energy & Environmental Science*. **2014**, 7, 3061–3068.

[24] J. Cao and F. Yan, *Energy & Environmental Science*. **2021**, 14, 1286–1325.

[25] R. Ali, G. J. Hou, Z. G. Zhu, Q. B. Yan, Q. R. Zheng and G. Su, *Chem. Mat.*. **2018**, 30, 718–728.

[26] D. Cortecchia, H. A. Dewi, J. Yin, A. Bruno, S. Chen, T. Baikie, P. P. Boix, M. Grätzel, S. Mhaisalkar, C. Soci and N. Mathews, *Inorganic Chem.* **2016**. 55, 1044–1052.

[27] T. Wu, X. Liu, X. Luo, X. Lin, D. Cui, Y. Wang, H. Segawa, Y. Zhang and L. Han, *Joule*. **2021**, 5, 863–886.

[28] K. Nishimura, M. A. Kamarudin, D. Hirotani, K. Hamada, Q. Shen, S. Iikubo, T. Minemoto, K. Yoshino and S. Hayase, *Nano Energy*. **2020**, 74, 104858.

[29] M. A. Kamarudin, D. Hirotani, Z. Wang, K. Hamada, K. Nishimura, Q. Shen, T. Toyoda, S. Iikubo, T. Minemoto, K. Yoshino and S. Hayase, *J. Phys. Chem. Letters*. **2019**, 10, 5277–5283.

[30] S. M. Jain, T. Edvinsson and J. R. Durrant, *Comm. Chem.* **2019**, 2, 1–7.

[31] W. Jabeur, R. Msalmi, M. Korb, M. Holub, E. Mosconi, A. Tozri and N. A. Althubiti, *J. Mater Chem. C*. **2021**, 17158–17166.

[32] M. Bourwina, R. Msalmi, S. Walha, M. M. Turnbull, T. Roisnel, F. Costantino and E. Mosconi, *J. Mater Chem. C*. **2021**, 5970–5976.

[33] A. Elattar, H. Suzuki, R. Mishima, K. Nakao, H. Ota, T. Nishikawa, H. Inoue, A. K. K. Kyaw and Y. Hayashi, *J. Mater Chem. C*. **2021**, 9, 3264–3270.

[34] B. Vargas, E. Ramos, E. Pérez-Gutiérrez, J. C. Alonso and D. Solis-Ibarra, *Journal of the American Chemical Society*, **2017**, 139, 9116–9119.

[35] A. P. Ingle, P. Paralikar, S. Shende, I. Gupta, J. K. Biswas, L. H. Da Silva Martins and M. Rai, Biomedical Applications of Metals. **2018**, 95–112.

[36] X. P. Cui, K. J. Jiang, J. H. Huang, Q. Q. Zhang, M. J. Su, L. M. Yang, Y. L. Song and X. Q. Zhou, *Synthetic Metals.* **2015**, 209, 247–250.

[37] X. Li, X. Zhong, Y. Hu, B. Li, Y. Sheng, Y. Zhang, C. Weng, M. Feng, H. Han and J. Wang, *J. Phys. Chem. Letters*. **2017**, 8, 1804–1809.

[38] X. Li, B. Li, J. Chang, B. Ding, S. Zheng, Y. Wu, J. Yang, G. Yang, X. Zhong and J. Wang, *ACS Applied Energy Mater.* **2018**, 1, 2709–2716.

[39] A. Elattar, W. Li, H. Suzuki, T. Kambe, T. Nishikawa, A. K. K. Kyaw and Y. Hayashi, *Chemistry–A European Journal.* **2022**, e202104316.

[40] W. Zhang, Y. Sui, B. Kou, Y. Peng, Z. Wu, J. Luo, *Appl. Mater. Interfaces* **2019**, 12(8), 9141-9149.

[41] W. Travis, E. N. K. Glover, H. Bronstein, D. O. Scanlon and R. G. Palgrave, *Chem. Sci.* **2016**, 7, 4548–4556.

[42] Z. Xiao and Y. Yan, *Adv. Energy Mater.* **2017**, 7, 1701136.

[43] A. Martinelli, A. Ray, A. L. Abdelhady and F. Locardi, *Acta Crystallographica Section B: Structural Science, Crystal Engineering and Materials*. **2022**, 78, 425–435.

[44] W. Jabeur, R. Msalmi, M. Korb, M. Holub, E. Mosconi, E. Čižmár, A. Tozri, N. A. Althubiti and H. Naïli, Journal of Materials Chemistry C, 2021, 9, 17158–17166.

[45] I. Hamdi, Y. Khan, F. Aouaini, J. H. Seo, H. J. Koo, M. M. Turnbull, B. Walker and H. Naili, Journal of Materials Chemistry C, 2022, 10, 3738–3745.[46] P. Pandey, N. Sharma, R. A. Panchal, S. W. Gosavi and S. Ogale, *ChemSusChem*, **2019**, 12, 3742–3746.

[47] L. Atourki, E. Vega, B. Marí, M. Mollar, H. Ait Ahsaine, K. Bouabid and A. Ihlal, *Applied Surface Science*. **2016**, 371, 112–117.

[48] X. Zheng, Y. Liu, G. Liu, J. Liu, X. Ye, Q. Han, C. Ge and X. Tao, *Chem. Mater.* **2016**, 28, 4421–4431

[49] A. Jaffe, Y. Lin, W. L. Mao and H. I. Karunadasa, *Journal of the American Chemical Society*, **2015**, 137, 1673–1678.

[50] N. Balachandran, T. M. Robert, T. Jayalatha, P. M. Neema, D. Mathew and J. Cyriac, *Journal of Alloys and Compounds*. **2021**, 879, 160325.

[51] P. Yang, G. Liu, B. Liu, X. Liu, Y. Lou, J. Chen and Y. Zhao, Chemical Communications, 2018, 54, 11638–11641.

[52] Y. Wang, L. Duan, M. Zhang, Z. Hameiri, X. Liu, Y. Bai and X. Hao, *Solar RRL*. **2022**, 6, 2200234.

[53] Y. Yang, N. D. Pham, D. Yao, L. Fan, M. T. Hoang, V. T. Tiong, Z. Wang, H. Zhu and H. Wang, *ACS Appl. Mater. Interfaces* **2019**, 11, 28431–28441.

[54] (a) M. T. Khan, N. H. Hemasiri, S. Kazim, and S. Ahmad, *Sustain. Energy Fuels*. **2021**, 5, 6352-6360. (b) H. Dhifaoui, N. H. Hemasiri, W. Aloui, A. Bouazizi, S. Kazim, and S. Ahmad, *Adv. Mater. Interfaces*. **2021**, 8(22), 2101002.

[55] X. Zhang, X. Ren, B. Liu, R. Munir, X. Zhu, D. Yang, J. Li, Y. Liu, D. M. Smilgies, R. Li, Z. Yang, T. Niu, X. Wang, A. Amassian, K. Zhao and S. Liu, *Energy and Environmental Science*, **2017**, 10, 2095–2102.

[56] H. Tsai, W. Nie, J. C. Blancon, C. C. Stoumpos, R. Asadpour, B. Harutyunyan, A. J. Neukirch, R. Verduzco, J. J. Crochet, S. Tretiak, L. Pedesseau, J. Even, M. A. Alam, G. Gupta, J. Lou, P. M. Ajayan, M. J. Bedzyk, M. G. Kanatzidis and A. D. Mohite, *Nature*. **2016**, 536, 312–317.

[57] F. Guo, S. Qiu, J. Hu, H. Wang, B. Cai, J. Li, X. Yuan, X. Liu, K. Forberich, C. J. Brabec and Y. Mai, *Advanced Science*. **2019**, 6,1901067.

[58] N. H. Hemasiri, S. Kazim, L. Calio, S. Paek, M. Salado, G. Pozzi, L. Lezama, M. K. Nazeeruddin, and S. Ahmad, *ACS Appl. Mater. Interfaces*. **2020**, 12(8), 9395–9403